




Polarized electron acceleration in beam-driven plasma wakefield based on density down-ramp injection

Yitong Wu ^{1,2} Liangliang Ji,^{1,3,*} Xuesong Geng,¹ Qin Yu,¹ Nengwen Wang,¹ Bo Feng,¹ Zhao Guo,¹ Weiqing Wang,¹ Chengyu Qin,¹ Xue Yan,¹ Lingang Zhang,¹ Johannes Thomas,⁵ Anna Hützen ^{6,7} Alexander Pukhov,⁵ Markus Büscher ^{6,7} Baifei Shen,^{1,3,4,†} and Ruxin Li^{1,3,8,‡}

¹State Key Laboratory of High Field Laser Physics, Shanghai Institute of Optics and Fine Mechanics, Chinese Academy of Sciences, Shanghai 201800, China

²Center of Materials Science and Optoelectronics Engineering, University of Chinese Academy of Sciences, Beijing 100049, China

³CAS Center for Excellence in Ultra-intense Laser Science, Shanghai 201800, China

⁴Shanghai Normal University, Shanghai 200234, China

⁵Institut für Theoretische Physik I, Heinrich-Heine-Universität Düsseldorf, 40225 Düsseldorf, Germany

⁶Peter Grünberg Institut (PGI-6), Forschungszentrum Jülich, Wilhelm-Johnen-Str. 1, 52425 Jülich, Germany

⁷Institut für Laser- und Plasmaphysik, Heinrich-Heine-Universität Düsseldorf, 40225 Düsseldorf, Germany

⁸Shanghai Tech University, Shanghai 201210, China



(Received 27 June 2019; revised manuscript received 13 September 2019; published 11 October 2019)

We investigate the precession of electron spins during beam-driven plasma-wakefield acceleration based on density down-ramp injection by means of full three-dimensional (3D) particle-in-cell (PIC) simulations. A relativistic electron beam generated via, e.g., laser wakefield acceleration, serves as the driving source. It traverses the prepolarized gas target and accelerates polarized electrons via the excited wakefield. We derive the criteria for the driving beam parameters and the limitation on the injected beam flux to preserve a high degree of polarization for the accelerated electrons, which are confirmed by our 3D PIC simulations and single-particle modeling. The electron-beam driver is free of the prepulse issue associated with a laser driver, thus eliminating possible depolarization of the prepolarized gas due to ionization by the prepulse. These results provide guidance for future experiments towards generating a source of polarized electrons based on wakefield acceleration.

DOI: [10.1103/PhysRevE.100.043202](https://doi.org/10.1103/PhysRevE.100.043202)

I. INTRODUCTION

Wakefield acceleration driven by a particle beam (PWFA) [1–3] or a short laser pulse (LWFA) [4,5] promises acceleration gradients larger than GV/cm for electron acceleration. This is about three orders of magnitudes larger than the field gradients in traditional rf accelerators (~ 1 MV/cm) [6]. This makes wakefield acceleration a promising approach to develop compact electron sources. Recently, GeV-scale electron beams with total charge of tens of pC to several nC have been obtained in experiments for either LWFA [7,8] or PWFA [9]. Although many beam properties (e.g. energy spread, total charge, beam divergence) have been studied in depth [1,10,11], the spin polarization of electron has rarely been discussed in wakefield acceleration and no experimental data can be found in literature. In fact, spin-polarized electrons are widely used in nuclear physics, material science, and electron-positron colliders [12–14]. They are generally generated in a storage ring via radiative polarization [12] (the Sokolov-Ternov effect [15]), which takes about a few hours to build up the beam polarization. For this approach to be valid in wakefield acceleration, it is estimated that the required duration is at the ~ 1 - μ s level [16,17], corresponding

to an approximately kilometer-scale acceleration distance. Such requirement is beyond the availability of state-of-the-art wakefield acceleration. An alternative way to obtain energetic polarized electron beams is to extract prepolarized electrons directly from a polarized gas and then to accelerate them subsequently, for example in a Linac [14]. The first extraction process can be circumvented, if the polarized electrons are accelerated in a wakefield. However, this requires a fully prepolarized gas target with appropriate density.

By means of the ultraviolet (UV) photodissociation of hydrogen halide [18–23], gas densities reaching 10^{19} cm⁻³ could be achieved at full polarization of electrons in the hydrogen atoms, which is suitable for wakefield acceleration. A particular design based on such a technique has been given for the LWFA case [17]. The key issue to accelerate polarized electrons beams in a wakefield is to find a parameter regime that allows the preservation of all single-particle spins during the injection and the subsequent acceleration. The latter issue is rather unproblematic because the depolarization of a high energetic electron beam grows only slowly with the mean beam energy [24], while the first point requires a more precise examination. Previous works show that the depolarization happening in the injection phase can be mitigated by shifting the laser focal position to decrease the amount of injected beam charge [25]. Recently, a vortex laser driver has been proposed to produce energetic electrons of high polarization, without strongly reducing the loaded beam charge [17].

*jill@siom.ac.cn

†bfshen@mail.shnc.ac.cn

‡ruxinli@mail.siom.ac.cn

Compared to the LWFA scheme, PWFA [1,2,26] is promising for generation of high-energy electrons over longer acceleration distances because the driver does not suffer from laser-type diffraction and dephasing effects. Electron beams with an energy up to 85 GeV have been obtained by a 42-GeV driving electron beam [11]. An apparent advantage of PWFA for accelerating prepolarized electrons is that the driver does not contain a pedestal or a prepulse, as in the case of a laser driver. Thus, prepolarized targets do not confront possible depolarization issues from the ionization or heating associated with the laser case. As a matter of fact, the polarization of the initially spin-aligned electrons oscillates among the range 0~100% at a period of 350 ps [17,20]. Considering the nanosecond-scale duration of the prepulse for a typical high-power laser system, if ionization is induced by the laser prepulse, the spin orientations of electrons stripped out at different phases of the 350-ps oscillation period will be misaligned. The electron target would lose its polarization purity before the arrival of the main pulse. In order to minimize this effect in LWFA, the prepulse should be controlled below the ionization threshold, which is about 10^{12} W/cm² for typical gas targets like hydrogen [27]. Although the injection process in the density down ramp is similar to LWFA, a significant distinction appears in the beam or laser plasma-interaction stage in PWFA. In PWFA, background electrons are expelled via the electrostatic field generated by the drive beam. Typical field strength is at 10^{11} V/m [1,10,11], about two orders of magnitude smaller than the laser field in LWFA ($\sim 10^{13}$ V/m) [7,8]. Thus, the spin variation is not significant during the beam-interaction stage (before injection). In contrast, in LWFA the electron spin oscillates dramatically during the laser-interaction stage due to the much stronger laser field [17,25]. That creates risks for sudden depolarization if the laser field is not so evenly distributed, e.g., spin would gain net change after being averaged over the whole interaction duration. This unfavorable effect is inhibited in PWFA.

These benefits motivate the investigation of spin-polarized electron acceleration for a beam driver in the current work. Several kinds of beam sources are available for PWFA, such as proton [9,28], positron [29,30], and electron beams [11,26,31]. In this work, we restrict our discussion on electron-beam driven wakefield acceleration since the required beams are available either from Linacs such as the Stanford Linear Accelerator Center (SLAC) [11,26,31] or LWFA [7,8]. In particular, we choose density tailing target [32–37] to realize electron injection in the down ramp, where the setup for generating 100% prepolarized electron targets has been introduced in detail in our previous work [17]. It is worth mentioning that for other injection schemes such as Trojan Horse ionization injection and beam-induced ionization injection [38–40], the preparation of prepolarized target needs to be further explored. We derive the criteria to preserve the beam polarization and give the limitations on the injected beam flux. As an example, we use a typical high-energy electron beam from the LWFA process and successfully accelerate pre-polarized electrons with a polarization over 80%, in our three-dimensional (3D) particle-in-cell (PIC) simulations.

The paper is organized as follows: In Sec. II we introduce the basic setup for PWFA and the considered parameter range of plasma, driving source as well as the initial spin orienta-

tions chosen for simulations. In Sec. III we present typical simulations results. They serve as an example to understand the basic physical processes. In Sec. IV we derive the criteria for the driving source, the plasma setups, and the initial spin directions as well as the limitation for the injected beam peak current via theoretical analysis and compare the results with simulation results. Finally, in Sec. V, we give a brief summary.

II. SIMULATION SETUP

As described in Ref. [17], a specific design for a prepolarized electron target is based on UV photodissociation of HCl gas, which promises 100% polarization for electrons in the hydrogen atoms. The initial spin orientation can be adjusted by switching the directions of aligning and photodissociation light simultaneously. In this work we present PIC simulations with an energetic electron beam propagating along the x axis from the left boundary of the simulation window. The beam passes through the spin-polarized hydrogen gas, which can be fully ionized by the driving beam [11,41]. In order to match experimental conditions like those in Refs. [7,11], we assume that the electron beam density has a Gaussian profile $n_b(r, \xi = x - ct) = n_{b0} \exp(-r^2/2\sigma_r^2 - \xi^2/2\sigma_l^2)$, where the σ_l , σ_r are the longitudinal and transverse beam sizes (see Fig. 1), respectively, and n_{b0} denotes the peak density of the driving beam. The mean electron momentum is $2000 m_e c$ (energy close to 1 GeV), while the relative momentum spread is 10%. It is important to note that for a higher electron energy, the final energy of the accelerated beam is larger while the injection process is about the same. Since the spin variation mainly happens during injection, the energy of the driver has little effect on beam polarization. Therefore, we choose beam parameters accessible from either SLAC or LWFA. For efficient injection, a so-called density tailing target (also known as density down-ramp injection) [34–37] is utilized with ramp profile: $n(\kappa) = \{[\alpha - \Theta(\kappa)]\Theta(L - \kappa) \cos(\pi\kappa/2L) + \Theta(\kappa - L)\}n_0$ (see Fig. 1), where $\Theta(x)$ is the step function, $\kappa = x - x_p$, $x_p = 36 \mu\text{m}$, and $L = 16 \mu\text{m}$, respectively. $\alpha = n_p/n_0 = 4$ is the ratio between the peak density of the ramp and the background density.

We employ the classical spin model applying Ehrenfest's theorem [12] which describes the particle spin with direction vector s ($|s| = 1$). Initially all electron spins have the same direction, $s_0 = \cos \psi e_x + \sin \psi \cos \zeta e_y + \sin \psi \sin \zeta e_z$, where ζ and ψ are the azimuthal and polar angles of the vector s with respect to the x axis, as sketched in Fig. 1. Considering cylinder symmetry, it is natural to set $\zeta = 0$ so that $s_0 = \cos \psi e_x + \sin \psi e_y$, with the averaged initial polarization $P_0 = |\Sigma s_0|/N = 1$ while $P_{x0} = |\Sigma s_{x0}|/N = \cos \psi$, $P_{y0} = |\Sigma s_{y0}|/N = \sin \psi$, and $P_{z0} = |\Sigma s_{z0}|/N = 0$, respectively. In our PIC simulations, we vary the driver parameters such that $\sigma_r = 0.5 \sim 3 \mu\text{m}$, $\sigma_l = 0.8 \sim 5.5 \mu\text{m}$, $n_{b0} = 0.5 \sim 2.5 \times 10^{19} \text{cm}^{-3}$; the plasma density is $n_0 = 0.5 \sim 2.5 \times 10^{18} \text{cm}^{-3}$ and $\alpha = 2 \sim 8$, respectively. The initial spin orientation is defined by the angle $\psi = 0 \sim \pi/2$. A moving window is employed with a $48 \mu\text{m}(x) \times 48 \mu\text{m}(y) \times 48 \mu\text{m}(z)$ -sized simulation box and $1200 \times 600 \times 600$ cells.

In general, spin dynamics contains three parts [12]: the Stern-Gerlach force (the gradient force), the Sokolov-Ternov effect (spin flip) [15], and spin precession in electric and

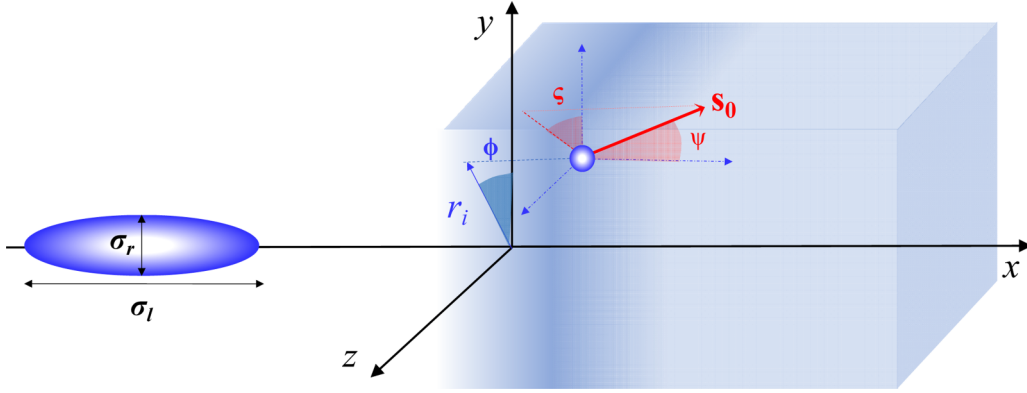


FIG. 1. Sketch of the electron beam-driven wakefield acceleration: the driving beam has a longitudinal size σ_l and transverse size σ_r ; plasma target comprises a density ramp and background density; electron is injected at the location defined by the transverse radius of r_i and azimuthal angle ϕ ; the electron spin vector orientation is defined by the azimuthal angle ζ and polar angle ψ .

magnetic fields according to the Thomas-Bargmann-Michel-Telegdi (T-BMT) equation. However, during wakefield acceleration, the Stern-Gerlach force is much smaller than the Lorentz force [16,17,42] and the polarization time of spin flip is much larger than typical wakefield acceleration processes [16,17]. Therefore, we only consider the T-BMT equation for spin dynamics and implement it into the VLPL code [43] following the form [44]

$$ds/dt = \mathbf{\Omega} \times \mathbf{s}, \quad (1)$$

with $\mathbf{\Omega} = \frac{e}{m}(\frac{1}{\gamma}\mathbf{B} - \frac{\beta}{\gamma+1} \times \frac{\mathbf{E}}{c}) + a_e \frac{e}{m}(\mathbf{B} - \frac{\gamma}{\gamma+1}\boldsymbol{\beta}(\boldsymbol{\beta} \cdot \mathbf{B}) - \boldsymbol{\beta} \times \frac{\mathbf{E}}{c})$. Here m is the electron mass; $\boldsymbol{\beta}$ is the electron velocity normalized by c (velocity of light in vacuum); $\gamma = 1/(1-\beta^2)^{-1/2}$ is the relativistic factor; $a_e = (g-2)/2 \approx 1.16 \times 10^{-3}$ (g is the gyromagnetic factor); and the vector \mathbf{s} is the electron spin in its rest frame [2], respectively. We added the T-BMT equation to the moving particle module and calculate $\mathbf{\Omega}$ as well as the spin-vector component parallel (s_{\parallel}) and perpendicular (s_{\perp}) to $\mathbf{\Omega}$ for each particle at every time step. To eliminate numerical errors, Eq. (1) is solved by the rotation matrix method.

III. SIMULATION RESULTS

As an example, we first choose the driving beam of $\sigma_r = 2 \mu\text{m}$, $\sigma_l = 2.5 \mu\text{m}$, $n_{b0} = 10^{19} \text{cm}^{-3}$ with $\alpha = 4$ and $n_0 = 10^{18} \text{cm}^{-3}$. The electron spins are initially aligned along the laser propagation direction $\mathbf{s}_0 = \mathbf{e}_x$, which is corresponding to $\psi = 0$. The total charge of the electron beam is about 250 pC. In Figs. 2(a) and 2(b), we show an isosurface plot of the electron density, the field distribution on the x - z plane, and electron density distribution on the x - y plane. A clean bubble is driven by the electron beam in the plasma. The simulations show an increased radius of the blowout region after the driving beam transverses the density peak. As a result, the electrons at the bubble tail [see Fig. 2(a) around $x = 30 \mu\text{m}$] can then be injected into the bubble. Those electrons are trapped and form a dense bunch that is subsequently accelerated to high energies.

The spin orientations of sample electrons in the bunch are denoted by black arrows. It is clear from Figs. 2(a) and

2(b) that the initially well-polarized electrons (arrows pointing along the x axis) are depolarized during injection, considering the parameter set we used. We notice that electrons are focused by both the transverse electric field E_r and the azimuthal magnetic field B_{ϕ} during injection. For nonrelativistic electrons ($\gamma \sim 1$ and $\beta \ll 1$), one knows that $\mathbf{\Omega} \propto \mathbf{B} \sim B_{\phi}$ from Eq. (1), so that B_{ϕ} predominates the precession. We give the B_{ϕ} distribution in Figs. 2(c) and 2(d), where one can see the strong magnetic field generated by the driving beam at 130 fs and later also with the injected electron beam at 260 fs. The magnetic field is associated with electron injection density (self-generated field) and background ion density (bubble-generated field), which will be evaluated in the next section.

Since the polarization of the beam originates from the statistic of the whole electron beam, we trace all accelerated electrons trapped by the bubble field and calculate the absolute value of polarization with $|P| = \sqrt{\sum_{\kappa} P_{\kappa}^2}$ where $P_{\kappa} = \sum_i s_{\kappa i}/N$ with $\kappa = x, y, z$ as well as the averaged relativistic factor $\bar{\gamma} = \sum_i \gamma_i/N$ at each time step. Here we define polarization with positive value if $\sum P_{\kappa} e_{\kappa} \cdot \mathbf{s}_0 > 0$ while negative value $\sum P_{\kappa} e_{\kappa} \cdot \mathbf{s}_0 < 0$. In particular, the beam polarization $P \approx P_x$ for $\mathbf{s}_0 = \mathbf{e}_x$ and $P \approx P_y$ for $\mathbf{s}_0 = \mathbf{e}_y$ [17,25] (see also Theoretical Analysis). We summarize the results for both cases at $\sigma_r = 2$ and $1 \mu\text{m}$ in Fig. 3. The polarization (solid lines) for all cases decreases significantly when γ is close to 1 ($t < 250$ fs), corresponding to the injection phase of the acceleration process. However, the polarization stays constant after about 300 fs, when the mean bunch energy is much larger than the electron rest energy ($\gamma \gg 1$) and thus it is in the steady acceleration phase. A comparison between the cases with different σ_r shows that the polarization is preserved at a very high level for the $\sigma_r = 1 \mu\text{m}$ cases ($\sim 67\%$ for $\mathbf{s}_0 = \mathbf{e}_x$ and $\sim 88\%$ for $\mathbf{s}_0 = \mathbf{e}_y$). In contrast to that, the electron beam is almost completely depolarized for $\sigma_r = 2 \mu\text{m}$, about -12% with $\mathbf{s}_0 = \mathbf{e}_x$ and 35% with $\mathbf{s}_0 = \mathbf{e}_y$, after 250 fs. The trend is also clearly seen from the spin distribution in Fig. 3(b). One sees most trapped electrons preserving $s_i \approx 1$ for $\sigma_r = 1 \mu\text{m}$ but spread out between -1 to 1 for $\sigma_r = 2 \mu\text{m}$, indicating lower polarization level for the latter. The results suggest that to preserve the electron polarization in PWFAs,

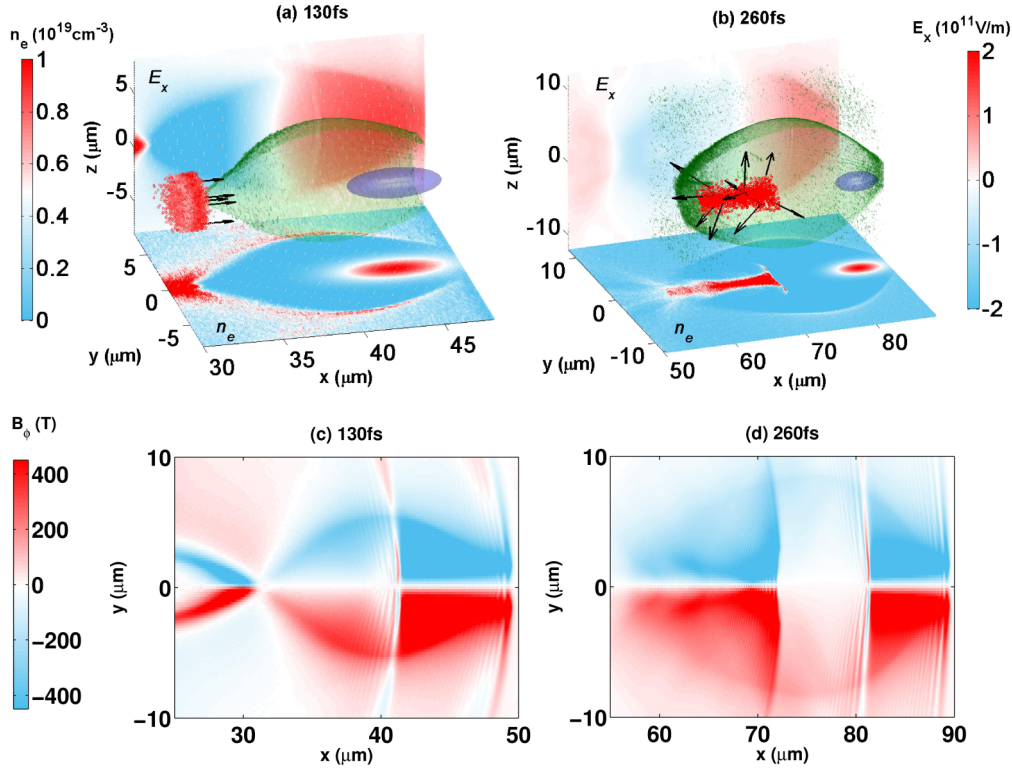


FIG. 2. Isosurface of the bubble (green, outside) and the driving beam (blue, inside) are shown in (a) and (b), respectively, where the electron density is projected onto the x - y (at $z = 0$) plane, while the longitudinal electric field E_x is projected onto the x - z plane (at $y = 0$). The black arrows denote the spin directions for electrons. The azimuthal magnetic field (B_ϕ) distributions at (c) 130 fs and 260 fs (d). Data are taken at the beginning (130 fs) and end (260 fs) of injection for the driving electron beam $\sigma_r = 2 \mu\text{m}$, $\sigma_l = 2.5 \mu\text{m}$, $n_{l0} = 1 \times 10^{19} \text{cm}^{-3}$ with $\alpha = 4$, $n_0 = 10^{18} \text{cm}^{-3}$, and $s_0 = e_x$.

certain restrictions must apply, which will be discussed in the following section.

IV. THEORETICAL ANALYSIS

The spin precession of electrons, known from Eq.(1), depends on the strength and direction of the angular frequency vector Ω . Typically we have $B \sim B_\phi$, $\beta \sim \beta_x$, $\beta \times E \sim E_r \beta_x e_\phi$ for the bubble regime [34,45], where B_ϕ is the azimuthal magnetic field, E_r is the radial electric field, and β_x is the normalized velocity along the x axis. Substituting $\gamma \ll 1/a_e$ in the early acceleration process, we have $\Omega = \frac{e}{m} (\frac{B_\phi}{\gamma} - \frac{\beta_x E_r}{\gamma+1} c) e_\phi$. With the rotation intrinsic of Eq. (1), $s_{\parallel} = (s \cdot e_\phi) e_\phi$ (component of the spin vector parallel to Ω) keeps constant while the perpendicular component $s_{\perp} = s - s_{\parallel}$ rotates in the x - r plane. Combining this with the initial condition $s_0 = \cos \psi e_x + \sin \psi e_y$, one obtains $s_{\parallel}(t=0) = \sin \psi (e_y \cdot e_\phi) e_\phi$, $s_{\perp}(t=0) = \cos \psi e_x + \sin \psi (e_y \cdot e_r) e_r$, so that $s = \sin \psi (e_y \cdot e_\phi) e_\phi + \cos(\Delta\theta_s) [\cos \psi e_x + \sin \psi (e_y \cdot e_r) e_r] + \sin(\Delta\theta_s) [\cos \psi e_r - \sin \psi (e_y \cdot e_r) e_x]$. Here e_x , e_r , and e_ϕ are normalized base vectors in cylindrical coordinates and the rotation angle $\Delta\theta_s \approx \langle \Omega \rangle \Delta t$ depends on the time-averaged precession frequency and the precession duration Δt . Considering the injected beam containing N particles with homogeneous density within the radius R and assuming all electrons are symmetrically distributed around the x axis, the polarization in each direction of the beam can

be derived as

$$P_\alpha(\alpha = x, y, z) = \sum_{i=1}^N \frac{s_i \cdot e_\alpha}{N} = \frac{1}{\pi R^2} \int_0^R \int_0^{2\pi} s_i k \cdot e_\alpha r dr d\phi. \quad (2)$$

Recalling $e_x \cdot e_\phi = 0$, $e_y \cdot e_\phi = -\sin \phi$, $e_z \cdot e_\phi = \cos \phi$, $e_x \cdot e_r = 0$, $e_y \cdot e_r = \cos \phi$, $e_z \cdot e_r = \sin \phi$, and noticing that $\Delta\theta_s$ is independent of ϕ , one obtains $P_x = \delta \cos \psi$, $P_y = (1 + \delta) \sin \psi / 2$, and $P_z = 0$, where δ is a statistic average factor for all trapped electrons relevant to $\Delta\theta_s$:

$$\delta = \frac{2}{R^2} \int_0^R \cos(\Delta\theta_s) r dr. \quad (3)$$

The beam polarization turns out to be

$$P = \frac{\sqrt{\sin^2 \psi (1 + 2\delta - 3\delta^2) + 4\delta^2}}{2}. \quad (4)$$

In particular, $P = P_x = \delta$ for $s_0 = e_x$ and $P = P_y = (1 + \delta)/2$ for $s_0 = e_y$ which is also the reason why we only give spin distributions along the particular prepolarized directions in Fig. 3(b). The peak value of the polarization appears at $\psi = k\pi/2$ ($dP/d\psi = 0$, $k = 0, 1, 2, \dots$), corresponding to $(1 + \delta)/2$ for odd numbers of k (transverse initial polarization $s_0 = e_y$) and δ for even numbers of k (parallel initial polarization $s_0 = e_x$), which suggests that the polarization of the beam is larger for transverse case ($\delta < 1$), in agreement with the simulation results in Fig. 3.

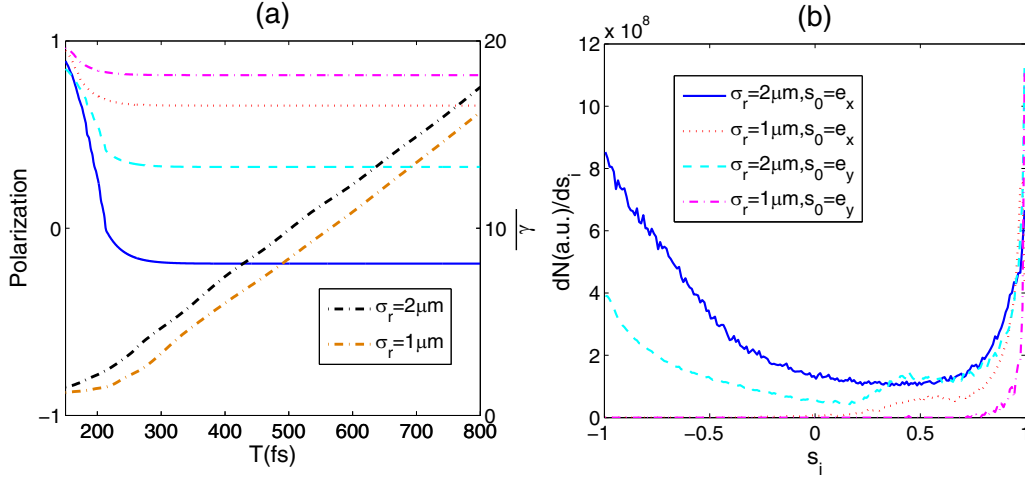


FIG. 3. Simulation results for trapped electrons located in the bubble. Displayed are the evolution for (a) beam polarization and the averaged relativistic factor of electron (dashed), (b) the spin s_i ($s_i = s_0$) distributions at 800 fs. In both figures, the blue solid lines and red dotted lines represent $\sigma_r = 2\mu\text{m}$ and $\sigma_r = 1\mu\text{m}$ with $s_0 = e_x$ while cyan dashed lines and pink dashed-dotted lines represent $s_0 = e_y$, respectively. Other parameters are the same where the $\sigma_l = 2.5\mu\text{m}$, $n_{b0} = 1 \times 10^{19}\text{cm}^{-3}$, $\alpha = 4$, and $n_0 = 10^{18}\text{cm}^{-3}$.

It should be noted that whatever initial spin directions are chosen, the beam polarization is restricted by δ which is relevant to the rotation angle of the spin for each particle. In fact, the rotation angle is only significant during the injection phase and negligible as soon as the electron bunch has a sufficiently high energy (see Fig. 3). This is because the Ω rapidly declines as γ increase. Substituting $E_r \sim cB_\phi$, $v \sim v_x = \beta_x c$, and $\gamma \gg 1$ for steady acceleration, the precession frequency can be simplified to $\Omega \approx eB_\phi/m\gamma(\gamma + 1) \sim 1/\gamma^2$. The acceleration time can be roughly estimated as $\Delta t = mc\gamma/eE_x$; thus, the rotation angle in this phase is about $\Delta\theta_s \sim cB_\phi/E_x\gamma \sim 1/\gamma \ll 1$, which can be ignored.

Therefore, we only need to evaluate δ during the injection phase. It depends on the injection position r_i , the injection time Δt_i , and strength of the averaged $\langle \Omega \rangle$ for each particle. For simplicity, the density of trapped electrons n_p is assumed to be homogeneous in the trapping area $r_i = 0 \sim r_b(x_p)$ with elapse time of $\Delta t_i = 4r_i/c$ [46–48] where r_b is the radius of the bubble. If the driver is an electron beam, r_b can be estimated by [34,45]

$$r_b^2(x) \approx 4\sigma_l\sigma_r \sqrt{\frac{n_{b0}}{n(x)}}. \quad (5)$$

Simulation results confirmed the evaluations from Eq. (5) [see Fig. 7(a) in the Appendix]. Recalling that $\langle \Omega \rangle$ is connected with B_ϕ , E_r , and β_x , following the Maxwell's equations:

$$\frac{1}{r} \frac{\partial}{\partial r} rB_\phi = -\frac{en_p\beta_x}{\epsilon_0 c} - \frac{\partial E_x}{c\partial \xi}, \quad (6a)$$

$$\frac{1}{r} \frac{\partial}{\partial r} rE_r = \frac{e[n(x) - n_p]}{\epsilon_0} - \frac{\partial E_x}{\partial \xi}. \quad (6b)$$

Assuming that all electrons experience the quasiconstant acceleration, it is possible to calculate the mean velocity $\langle \beta_x \rangle = \frac{1}{T} \int_0^T \beta_x dt = \beta_x(T)/2$. If we then substitute the characteristic time the electrons need to become relativistic, we see that $\langle \beta_x \rangle \sim 1/2$. Further, we find that $\gamma \sim 1$, $\langle n(x) \rangle \sim n_p/2$,

and $\langle \beta_x E_r \rangle \sim B_\phi/2$ during the injection. Substituting all these simplifications into $\langle \Omega \rangle$ yields $\langle \Omega \rangle \approx 3eB_\phi/4m$ which is only proportional to B_ϕ . Since the E_x decreases almost linearly [42], one has $\partial E_x/\partial \xi \approx n_0 e/2\epsilon_0$. To simplify the analysis, we ignore the temporal evolution of the density profile and consider averaged effects during the injection period; then, the averaged azimuthal magnetic field can be written as

$$B_\phi \approx \frac{(n_p + n_0)er}{4\epsilon_0 c}. \quad (7)$$

The results in simulations agree with Eq. (7) reasonably well [see Fig. 7(b) in the Appendix]. There are minor deviations at radius around $r_b(x_p)$ due to the focusing of the trapped beam, which is not included in our model. Combining Eq. (7) with $\langle \Omega \rangle \approx 3eB_\phi/4m$ and $\Delta t_i = 4r_i/c$, the rotation angle variation during injection is $\Delta\theta_s \approx 3eB_\phi r_i/mc \approx \eta r_i^2$ depending on the injection radius, with $\eta = 3e^2(n_0 + n_p)/4\epsilon_0 m_e c^2$.

As seen from Eq. (3), the diverged rotation angles $\Delta\theta_s$ of electrons injected from different radii define the beam polarization. One can find this from the single-particle modeling of selected electrons. In our calculation, the evolution of electron momenta is acquired from $\partial P_{er}/\partial t = F_r$, $\partial P_{ex}/\partial t = -eE_x$ where $F_r = -e(E_r - v_x B_\phi) = -e^2[(1 + \beta_x)n(x) - 2(1 - \beta_x^2)n_p]r/4\epsilon_0$ is the radial force derived from Eq. (6) and $E_x(\xi = x - ct) = -\int_\xi^0 en(y + ct)/2\epsilon_0 dy$ is the longitudinal electric field [34,49]. The spin dynamics are considered following the T-BMT equation using the magnetic field from Eq. (7). The calculated rotation angles $\Delta\theta_s$ at different injection radius $r_i = 0 \sim 3\mu\text{m}$ for $\sigma_r = 1\mu\text{m}$, $\sigma_l = 2.5\mu\text{m}$, $n_{b0} = 1 \times 10^{19}\text{cm}^{-3}$, $\alpha = 4$, and $n_0 = 10^{18}\text{cm}^{-3}$ are illustrated in Fig. 4(a). It is seen that the rotation angles are very small around the axis while much larger for electrons located farther away from the axis. Especially, the $\Delta\theta_s = \pi$ for $r_i = 3\mu\text{m}$ indicates the perpendicular component of the spin is almost flipped. Statistical average of the diverging rotation angles gives a low degree of polarization; therefore to retain the polarization

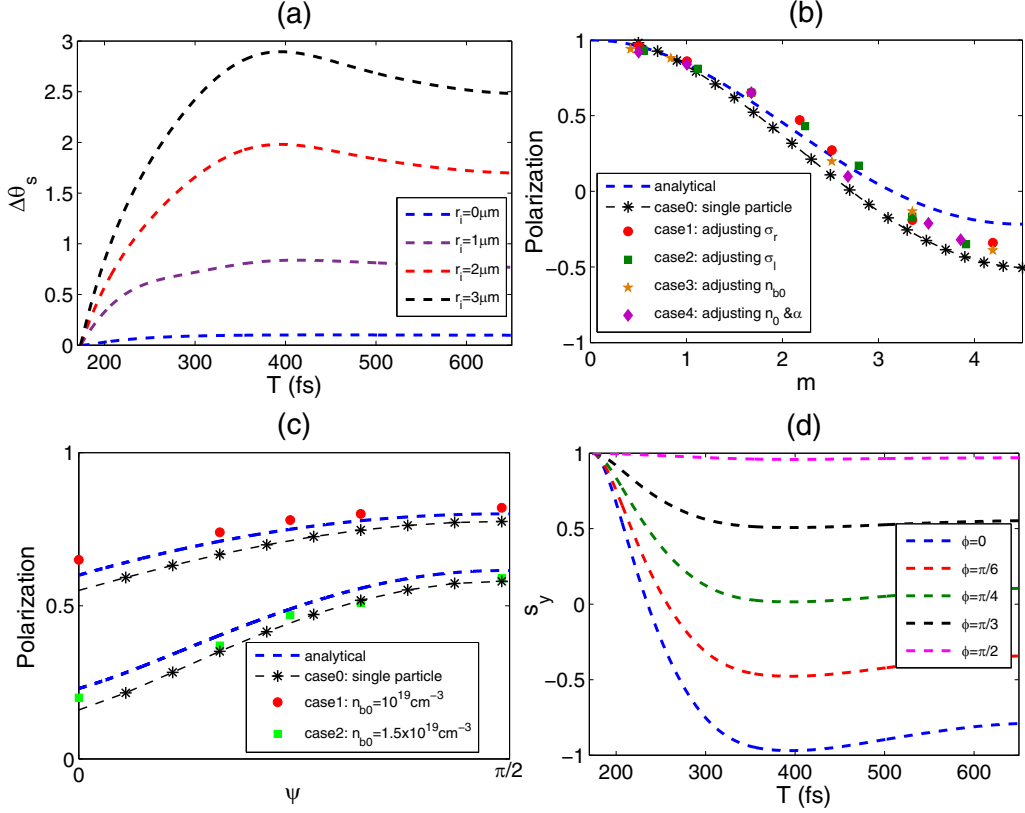


FIG. 4. (a) Evolution of the spin rotation angles $\Delta\theta_s$ based on single particle modeling for $r_i = 0 \sim 3 \mu\text{m}$ (lines from bottom to top) with the same parameters of the $\sigma_r = 2\text{-}\mu\text{m}$ case in Fig. 2. The polarization as a function of (b) the dimensionless parameter m [Eq. (9)] for initial spin $s_0 = \mathbf{e}_x$ and (c) ψ (initial spin directions parameters). In (b), the blue dashed line is the analytical results from Eq. (8); case 1 \sim 3 corresponds to adjusting σ_r at $\sigma_l = 2.5 \mu\text{m}$, $n_{b0} = 1 \times 10^{19} \text{cm}^{-3}$, σ_l at $\sigma_r = 1 \mu\text{m}$, $n_{b0} = 1 \times 10^{19} \text{cm}^{-3}$, and n_{b0} at $\sigma_l = 2.5 \mu\text{m}$, $\sigma_r = 1 \mu\text{m}$, respectively, with $\alpha = 4$, $n_0 = 10^{18} \text{cm}^{-3}$; case 4 denotes varying plasma density n_0 and α with $\sigma_l = 2.5 \mu\text{m}$, $\sigma_r = 1 \mu\text{m}$, $n_{b0} = 1 \times 10^{19} \text{cm}^{-3}$; case 0 represents the single-particle modeling for parameters in the region: $\sigma_l = 0.5 \sim 5 \mu\text{m}$, $\sigma_r = 0.5 \sim 5 \mu\text{m}$, $n_{b0} = 0.2 \sim 2 \times 10^{19} \text{cm}^{-3}$, $\alpha = 2 \sim 8$ and $n_0 = 0.2 \sim 2 \times 10^{18} \text{cm}^{-3}$. In (c), the blue dashed line is the analytical results from Eq. (4); Case 1 and 2 are for simulations with $n_{b0} = 1 \times 10^{19} \text{cm}^{-3}$ and $1.5 \times 10^{19} \text{cm}^{-3}$, respectively, with $\sigma_l = 2.5 \mu\text{m}$, $\sigma_r = 1 \mu\text{m}$, $\alpha = 4$, and $n_0 = 10^{18} \text{cm}^{-3}$. Case 0 represents the single-particle modeling with the same parameters of case 1 and 2. (d) The s_y evolution ($s_0 = \mathbf{e}_y$) for different $\phi = 0 \sim \pi/2$ (lines from bottom to top) of $r_i = 3 \mu\text{m}$ with the same parameters of (a) based on single-particle modeling.

purity, all injected electrons should keep their spin rotation angles sufficiently small, i.e., the spin precession frequencies must be kept low enough to make sure they rarely change during the injection time window.

Based on the above analysis, the key parameter of the beam polarization δ can be derived as

$$\delta = \int_0^{r_b(x_p)} 2\cos(\eta r^2) r dr / r_b^2 = \text{sinc}(m). \quad (8)$$

Here, $\text{sinc}(x) = \sin(x)/x$ and m is a dimensionless parameter defined by the total particle number of driving beam $N_d = (2\pi)^{3/2} \sigma_r^2 \sigma_l n_{b0}$ and transverse beam size σ_r ,

$$m = \eta r_b^2(x_p) = 3\sqrt{\frac{2}{\pi}} \frac{\alpha + 1}{\sqrt{\alpha}} \frac{r_e N_d}{\sigma_r} \sqrt{\frac{n_0}{n_{b0}}} \approx 6.7 \frac{g(\alpha) N_d [10^9]}{k \sigma_r [\mu\text{m}]}, \quad (9)$$

where $r_e = e^2/4\pi\epsilon_0 m_e c^2$ is classical electron radius, $g(\alpha) = (\alpha + 1)/\alpha^{1/2}$ with $\alpha = n_p/n_0$, $k = (n_{b0}/n_0)^{1/2}$. The beam polarization as a function of m is summarized in Fig. 4(b) for different combinations of the beam parameters, plasma

densities in the $s_0 = \mathbf{e}_x$ case. As mentioned in this section previously, the beam polarization $P = P_x = \delta$ for $s_0 = \mathbf{e}_x$, which is just described by Eq. (8). Compared with 3D PIC simulations and single-particle modeling, the analytical model is in good agreement overall. Small deviations appear for $m > 2$, which is caused by the usage of averaged values.

The beam polarization is also related to the initial spin direction known from Eq. (4), as given in Fig. 4(c) (ψ denotes the initial spin orientation). PIC simulations and single-particle calculations are consistent with the prediction of Eq. (4). One notices that the polarization increases with ψ in the region $[0, \pi/2]$, suggesting stronger restrictions for $\psi = 0$ (longitudinal polarization). According to Eq. (1), only the perpendicular component s_\perp changes during acceleration. It is relevant to ψ and ϕ (the angular displacement of the electron from its initial position, see Fig. 1) by $|s_\perp| = \sqrt{1 - \sin^2\psi \sin^2\phi}$. Therefore, the spin variations are not the same even electrons are injected at a fixed radius. To conceptualize this, we choose the particular case with $\psi = \pi/2$ ($s_0 = \mathbf{e}_y$) where the influence of ϕ on $|s_\perp|$ is most significant. The evolution of s_y for $r_i = 3 \mu\text{m}$ with azimuthal

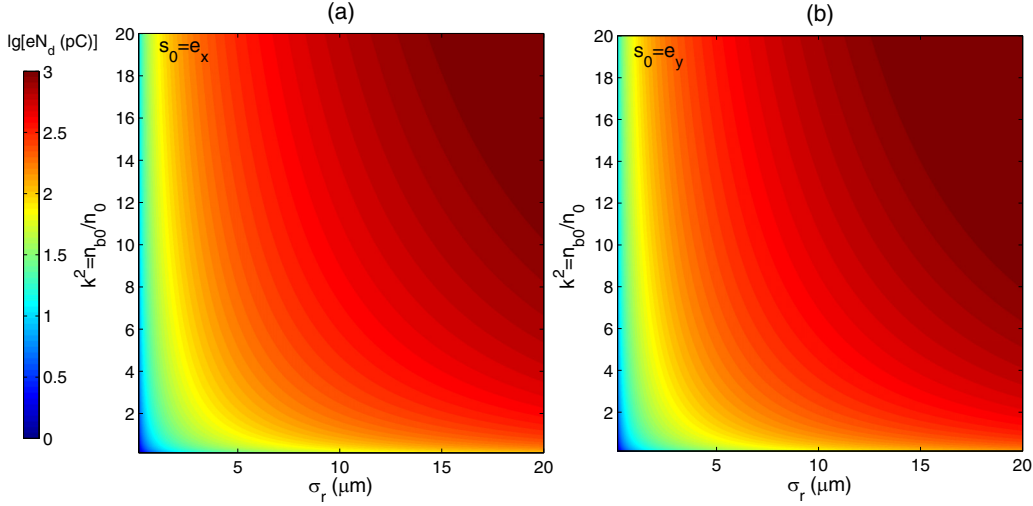


FIG. 5. Restrictions on the total particle number of the driving beam N_d to obtain beam polarization $>80\%$ for (a) longitudinal ($s_0 = e_x$) and (b) transverse polarization ($s_0 = e_y$), under certain k^2 and σ_r with $\alpha = 4$ based on Eq. (10). The color bar denotes for the maximum driven-beam total charge $Q = eN_d$ to obtain polarization $>80\%$.

angles $\phi = 0 \sim \pi/2$ is depicted in Fig. 4(d) based on the single-particle modeling. One sees that the s_y changes dramatically for $\phi = 0$ (corresponding to $|s_\perp| = 1$, spin direction is perpendicular to Ω) while preserving the initial value for $\phi = \pi/2$ (corresponding to $|s_\perp| = 0$, spin direction is parallel to Ω) during the whole acceleration. Since the perpendicular component is much smaller for higher $\phi \in [0, \pi/2]$, the spin variation is less significant accordingly.

In general, Eqs. (4) and (8) and Fig. 4 predict that high-polarization ($>80\%$) electron beams can be obtained by requiring the dimensionless parameter $m < 1.68$ for transverse aligning while $m < 1.45$ for longitudinal aligning. Thus from Eq. (9), the restriction for the driving electron beam is

$$\frac{g(\alpha)N_d[10^9]}{k\sigma_r[\mu\text{m}]} \leq 0.22(s_0 = e_x), \quad (10a)$$

$$\frac{g(\alpha)N_d[10^9]}{k\sigma_r[\mu\text{m}]} \leq 0.25(s_0 = e_y) \quad (10b)$$

From Eq. (10), specific restrictions apply for the beam charge, radius, and the density ratio between the driving beam and the background plasma, to get a higher degree of polarization. For example, $\sigma_r = 2 \mu\text{m}$, $\sigma_l = 2.5 \mu\text{m}$, $n_{b0} = 10^{19} \text{cm}^{-3}$ with $\alpha = 4$, $n_0 = 10^{18} \text{cm}^{-3}$, and $s_0 = e_x$ ($s_0 = e_y$) corresponds to $m \approx 3.5$ where the polarization is only $-0.1(0.4)$ from Eq. (4) while switching σ_r to $1 \mu\text{m}$ corresponds to $m \approx 1.7$ where the polarization is about $0.6(0.8)$ in agreement with the simulation results shown in Figs. 2 and 3. Moreover, the total number N_d (or the beam charge $Q = eN_d$) should meet the criteria suggested by Eq. (10) once k and σ_r are determined. To achieve polarizations $>80\%$, the total charge of the drive beam is restricted as a function of drive-beam size and the density factor k , as shown in Fig. 5. It is not surprising to see that larger beam size allows for higher beam charge, since the magnetic field is directly related to the current density.

Until now, we have derived the restrictions for the driven beam and plasma parameters to preserve injected electron-beam polarization. These naturally pose limitations for the injected beam flux. A rough estimation of the peak current of injected electrons can be applied as $I_{\text{peak}} \sim \alpha \pi n_0 c r_b^2(x_p) \sim \alpha \text{cm}/3(\alpha + 1)r_e$.

Recalling Eq. (4) and Eq. (8), the relationship between the beam polarization and peak current follows:

$$P(s_0 = e_x) \approx \text{sinc}\left(0.18 \frac{\alpha + 1}{\alpha} I_{\text{peak}}[\text{kA}]\right), \quad (11a)$$

$$P(s_0 = e_y) \approx \frac{1}{2} + \frac{1}{2} \text{sinc}\left(0.18 \frac{\alpha + 1}{\alpha} I_{\text{peak}}[\text{kA}]\right), \quad (11b)$$

for longitudinal and transverse polarization. We compare Eq. (11) with simulation results in Fig. 6 for various sets of parameters. In Figs. 6(a) and 6(b), both the theoretical analysis and PIC simulations show that the beam polarization declines when the flux increases. Specifically, the flux is limited to 5 kA for longitudinal polarization and ~ 7.5 kA for transverse polarization at 80% beam polarization, which is at the same order compared to LWFA [17,25]. Moreover, according to Eq. (11), one notices that the beam flux is only related to the parameter α at a fixed degree of polarization. The beam flux is significantly higher when the ratio between the peak density of the ramp and the background density is large, as seen in Figs. 6(c) and 6(d).

V. CONCLUSIONS

In conclusions, we considered a scheme to generate ultra-short polarized beams via PWFA. By means of PIC simulations incorporating the spin dynamics, we found that it is possible to acquire electron beams with high polarization by controlling the driving-beam parameters and plasma densities at various initial spin directions. We developed an efficient analytical model that interprets the PIC simulations very

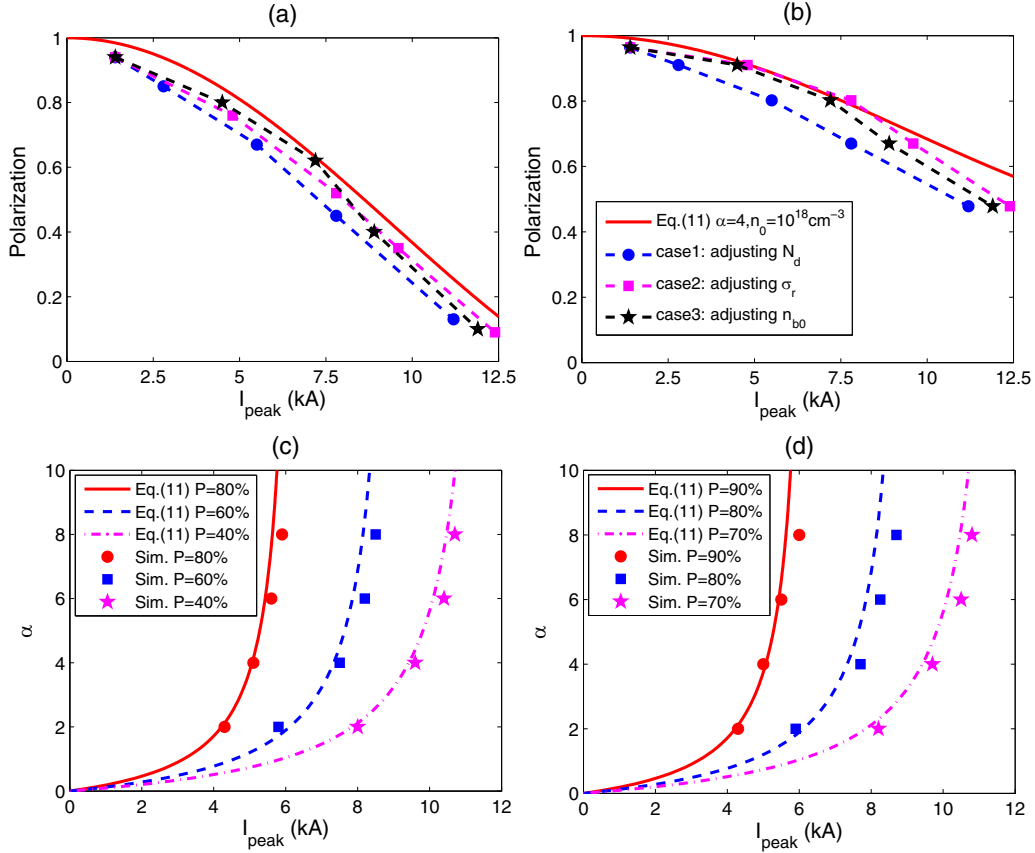


FIG. 6. Polarization as a function of the peak current I_{peak} under certain plasma densities with $\alpha = 4$ and $n_0 = 10^{18} \text{ cm}^{-3}$ for (a) longitudinal ($s_0 = e_x$) and (b) transverse ($s_0 = e_y$) polarization. The red lines represent results predicted by Eq. (11) while case 1 \sim 3 (blue circles, pink squares, and black stars) denote simulation results adjusting N_d ($\sigma_r = 1 \mu\text{m}$, $k^2 = n_{b0}/n_0 = 5$), σ_r ($N_d = 2 \times 10^8$, $k^2 = n_{b0}/n_0 = 5$) and n_{b0} ($N_d = 2 \times 10^8$, $\sigma_r = 1 \mu\text{m}$) respectively. The beam flux as a function of α at fixed polarization values for (c) longitudinal and (d) transverse polarization, with fixed drive-beam parameters ($N_d = 2 \times 10^8$, $\sigma_r = 1 \mu\text{m}$, $n_{b0} = 5 \times 10^{18} \text{ cm}^{-3}$).

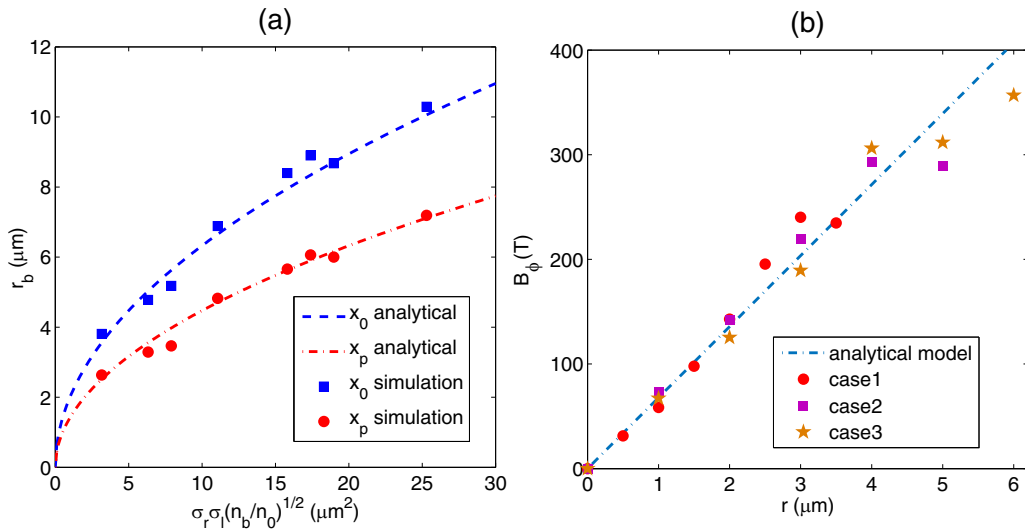


FIG. 7. (a) Radii of the beam-driven bubble under different parameters at $x = x_p$ (red, lower) and $x = x_0 = x_p + L$ (blue, upper), from Eq. (5) (dashed) and simulations (square and circle). (b) Azimuthal magnetic field B_ϕ as a function of the radius. The B field is averaged among the trapping region during the injection process. Analytical results from Eq. (7) are shown by the blue dotted-dashed line. Simulation results are given for case 1 (red circles): $\sigma_l = 2.5 \mu\text{m}$, $\sigma_r = 1 \mu\text{m}$, $n_{b0} = 1 \times 10^{19} \text{ cm}^{-3}$; case 2 (purple squares): $\sigma_l = 2.5 \mu\text{m}$, $\sigma_r = 2 \mu\text{m}$, $n_{b0} = 1 \times 10^{19} \text{ cm}^{-3}$, and case 3 (yellow stars): $\sigma_l = 2.5 \mu\text{m}$, $\sigma_r = 1 \mu\text{m}$, $n_{b0} = 5 \times 10^{19} \text{ cm}^{-3}$, respectively. For all cases $\alpha = 4$ and $n_0 = 10^{18} \text{ cm}^{-3}$.

well. The polarization of the accelerated beam is defined by a dimensionless parameter m , which is proportional to $g(\alpha)N_d/k\sigma_r$. Furthermore, the injected beam current is also limited to maintain high polarization. Besides, we stress that stronger restrictions apply for electron spins aligned parallel rather than perpendicular. These results can guide future experiments for generating polarized electron beams via plasma-wakefield acceleration.

ACKNOWLEDGMENTS

This work is supported by the Strategic Priority Research Program of Chinese Academy of Sciences (Grant No. XDB 16010000), the National Science Foundation of China (Grant No. 11875307), and the Recruitment Program for Young

Professionals. The German authors acknowledge support through the HGF-ATHENA project.

APPENDIX: COMPARISON BETWEEN EQS. (5) AND (7) AND SIMULATION RESULTS

To testify Eq. (5), we record the radii of the bubble in the density ramp and the constant density region for different parameters and compare the results from Eq. (5) with the simulation results in Fig. 7(a), where excellent match is found between the two. In order to assess the accuracy of Eq. (7), comparisons have been made with the azimuthal magnetic field in simulations, which is obtained by averaging values from the beginning of the injection to the end of the process. As exhibited in Fig. 7(b), the results in these simulations agree with Eq. (7) reasonably well.

-
- [1] P. Chen, J. M. Dawson, R. W. Huff, and T. Katsouleas, Acceleration of Electrons by the Interaction of a Bunched Electron Beam with a Plasma, *Phys. Rev. Lett.* **54**, 693 (1985); **55**, 1537(E) (1985).
- [2] C. Joshi, B. Blue, C. E. Clayton *et al.*, High energy density plasma science with an ultrarelativistic electron beam, *Phys. Plasmas* **9**, 1845 (2002).
- [3] E. Esarey, P. Sprangle, J. Krall *et al.*, Overview of plasma-based accelerator concepts, *IEEE Trans. Plasma Sci.* **24**, 252 (1996).
- [4] T. Tajima and J. M. Dawson, Laser Electron Accelerator, *Phys. Rev. Lett.* **43**, 267 (1979).
- [5] E. Esarey, C. B. Schroeder, and W. P. Leemans, Physics of laser-driven plasma based electron accelerators, *Rev. Mod. Phys.* **81**, 1229 (2009).
- [6] A. W. Chao, K. H. Mess, M. Tigner *et al.*, *Handbook of Accelerator Physics and Engineering Beam Cooling* (World Scientific, Singapore, 2013).
- [7] A. J. Gonsalves, K. Nakamura, J. Daniels *et al.*, Petawatt Laser Guiding and Electron Beam Acceleration to 8 GeV in a Laser-Heated Capillary Discharge Waveguide, *Phys. Rev. Lett.* **122**, 084801 (2019).
- [8] W. P. Leemans, A. J. Gonsalves, H. S. Mao *et al.*, Multi-GeV Electron Beams from Capillary-Discharge-Guided Subpetawatt Laser Pulses in the Self-Trapping Regime, *Phys. Rev. Lett.* **113**, 245002 (2014).
- [9] E. Adli, A. Ahuja, O. Apsimon *et al.*, Acceleration of electrons in the plasma wakefield of a proton bunch, *Nature (London)* **561**, 363 (2018).
- [10] C. G. R. Geddes, C. Toth, J. V. Tilborg *et al.*, High-quality electron beams from a laser wakefield accelerator using plasma-channel guiding, *Nature (London)* **431**, 538 (2004).
- [11] I. Blumenfeld, C. E. Clayton, F. J. Decker *et al.*, Energy doubling of 42 GeV electrons in a metre-scale plasma wakefield accelerator, *Nature (London)* **445**, 741 (2007).
- [12] S. R. Mane, Y. M. Shatunov, and K. Yokoya, Spin-polarized charged particle beams in high-energy accelerators, *Rep. Prog. Phys.* **68**, 1997 (2005).
- [13] T. J. Gay, Physics and technology of polarized electron scattering from atoms and molecules, *Advances in Atomic, Molecular, and Optical Physics*, Vol. 57 (Academic, New York, 2009), Chap. 4, pp. 157–247.
- [14] P. S. Farago, Electron spin polarization, *Rep. Prog. Phys.* **34**, 1055 (2002).
- [15] A. A. Sokolov and I. M. Ternov, Synchrotron radiation, *Sov. Phys. J.* **10**, 39 (1967).
- [16] J. Thomas, A. Hützen, A. Lehrach, A. Pukhov, L. Ji, Y. Wu, and M. Büscher, Spin-polarized particle beams from laser-plasma accelerators (unpublished).
- [17] Y. T. Wu, L. L. Ji, and X. S. Geng *et al.*, Polarized electron-beam acceleration driven by vortex laser pulses, *New J. Phys.* **21**, 073052 (2019).
- [18] D. Sofikitis, P. Glodic, G. Koumarianou *et al.*, Highly Nuclear-Spin-Polarized Deuterium Atoms from the UV Photodissociation of Deuterium Iodide, *Phys. Rev. Lett.* **118**, 233401 (2017).
- [19] D. Sofikitis, L. Rubio-Lago, L. Bougas *et al.*, Laser detection of spin-polarized hydrogen from HCl and HBr photodissociation: Comparison of H- and halogen-atom polarizations, *J. Chem. Phys.* **129**, 144302 (2008).
- [20] A. Hützen, J. Thomas, J. Böker *et al.*, Polarized proton beams from laser-induced plasmas, *High Power Laser Sci. Eng.* **7**, e16 (2019).
- [21] T. P. Rakitzis, P. C. Samartzis, R. L. Toomes *et al.*, Spin polarized hydrogen atoms from molecular photodissociation, *Science* **300**, 1936 (2003).
- [22] T. P. Rakitzis, Pulsed-Laser Production and Detection of Spin-Polarized Hydrogen Atoms, *Eur. J. Chem. Phys. Phys. Chem.* **5**, 1489 (2004).
- [23] D. Sofikitis, C. S. Kannis, G. K. Boulogiannis *et al.*, Ultrahigh-density Spin-polarized H and D Observed via Magnetization Quantum Beats, *Phys. Rev. Lett.* **121**, 083001 (2018).
- [24] J. Vieira, C.-K. Huang, W. B. Mori, and L. O. Silva, Polarized beam conditioning in plasma based acceleration, *Phys. Rev. Accel. Beams* **14**, 071303 (2011).
- [25] M. Wen, M. Tamburini, and C. H. Keitel, Polarized Laser-Wakefield-Accelerated Kiloampere Electron Beams, *Phys. Rev. Lett.* **122**, 214801 (2019).
- [26] A. Deng, O. S. Karger, T. Heinemann *et al.*, Generation and acceleration of electron bunches from a plasma photocathode, *Nat. Phys.* (2019).

- [27] R. M. Potvliege and R. Shakeshaft, Multiphoton processes in an intense laser field: Harmonic generation and total ionization rates for atomic hydrogen, *Phys. Rev. A* **40**, 3061 (1989).
- [28] A. Caldwell, K. Lotov, A. Pukhov *et al.*, Proton driven plasma wakefield acceleration, *Nat. Phys.* **5**, 363 (2009).
- [29] S. Gessner, E. Adli, and J. M. Allen, Demonstration of a positron beam-driven hollow channel plasma wakefield accelerator, *Nat. Commun.* **7**, 11785 (2016).
- [30] W. B. Mori, W. An, P. Muggli, and S. F. Pinkerton, Electron acceleration via positron driven plasma wakefield accelerator, *Conf. Proc. C110328*, 295 (2011).
- [31] M. Litos, E. Adli, W. An *et al.*, High-efficiency acceleration of an electron beam in a plasma wakefield accelerator, *Nature (London)* **515**, 92 (2014).
- [32] S. Bulanov, N. Naumova, F. Pegoraro *et al.*, Particle injection into the wave acceleration phase due to nonlinear wake wave breaking, *Phys. Rev. E* **58**, 5257(R) (1998).
- [33] H. Suk, N. Barov, J. B. Rosenzweig, and E. Esarey, Plasma Electron Trapping and Acceleration in a Plasma Wake Field Using a Density Transition, *Phys. Rev. Lett.* **86**, 1011 (2001).
- [34] K. V. Lotov, Blowout regimes of plasma wakefield acceleration, *Phys. Rev. E* **69**, 046405 (2004).
- [35] A. Gonsalves, K. Nakamura, C. Lin *et al.*, Tunable laser plasma accelerator based on longitudinal density tailoring, *Nat. Phys.* **7**, 862 (2011).
- [36] K. Schmid, A. Buck, C. M. S. Sears, J. M. Mikhailova, R. Tautz, D. Herrmann, M. Geissler, F. Krausz, and L. Veisz, Density-transition based electron injector for laser driven wakefield accelerators, *Phys. Rev. ST Accel. Beams* **13**, 091301 (2010).
- [37] A. Buck, K. Schmid, J. Xu *et al.*, Shock-Front Injector for High-Quality Laser-Plasma Acceleration, *Phys. Rev. Lett.* **110**, 185006 (2013).
- [38] B. Hidding, J. B. Rosenzweig, Y. Xi *et al.*, Beyond injection: Trojan horse underdense photocathode plasma wakefield acceleration, in *Advanced Accelerator Concepts: 15th Advanced Accelerator Concepts Workshop*, edited by R. Zgadzaj, E. Gaul, and M. C. Downer, AIP Conf. Proc. No. 1507 (AIP, Melville, New York, 2012), p. 570.
- [39] S. Z. Green, E. Adli, C. I. Clarke *et al.*, Laser ionized preformed plasma at FACET, *Plasma Phys. Controlled Fusion* **56**, 084011 (2014).
- [40] B. Hidding, G. Pretzler, J. B. Rosenzweig *et al.*, Ultracold Electron Bunch Generation via Plasma Photocathode Emission and Acceleration in a Beam-Driven Plasma Blowout, *Phys. Rev. Lett.* **108**, 035001 (2012).
- [41] D. Bruhwiler, D. A. Dimitrov, J. R. Cary *et al.*, Particle-in-cell simulations of tunneling ionization effects in plasma-based accelerators, *Phys. Plasmas* **10**, 2022 (2003).
- [42] M. Wen, C. H. Keitel, and H. Bauke, Spin-one-half particles in strong electromagnetic fields: Spin effects and radiation reaction, *Phys. Rev. A* **95**, 042102 (2017).
- [43] A. Pukhov, Three-dimensional electromagnetic relativistic particle-in-cell code VLPL (Virtual Laser Plasma Lab), *J. Plasma Phys.* **61**, 425 (1999).
- [44] V. Bargmann, L. Michel, and V. L. Telegdi, Precession of the Polarization of Particles Moving in a Homogeneous Electromagnetic Field, *Phys. Rev. Lett.* **2**, 435 (1959).
- [45] A. A. Golovanov, I. Yu. Kostyukov, J. Thomas, and A. Pukhov, Analytic model for electromagnetic fields in the bubble regime of plasma wakefield in non-uniform plasmas, *Phys. Plasmas* **24**, 103104 (2017).
- [46] S. Kalmykov, A. Beck, S. A. Yi, V. Khudik, M. C. Downer, E. Lefebvre, B. A. Shadwick, and D. P. Umstadter, Electron self-injection into an evolving plasma bubble: Quasi-monoenergetic laser-plasma acceleration in the blowout regime, *Phys. Plasmas* **18**, 056704 (2011).
- [47] S. Kalmykov, S. A. Yi, V. Khudik, and G. Shvets, Electron Self-injection and Trapping into an Evolving Plasma Bubble, *Phys. Rev. Lett.* **103**, 135004 (2009).
- [48] K. Swanson, H.-E. Tsai, S. Barber, R. Lehe, H.-S. Mao, S. Steinke, J. V. Tilborg, C. G. R. Geddes, and W. P. Leemans, Electron beam control using shock-induced density downramp injection, in *Advanced Accelerator Concepts: 17th Advanced Accelerator Concepts Workshop*, edited by S. H. Gold, G. S. Nusinovich, and K. P. Wootton, AIP Conf. Proc. No. 1812 (AIP, Melville, New York, 2017), p. 040004.
- [49] J. Thomas, I. Y. Kostyukov, J. Pronold *et al.*, Non-linear theory of a cavitated plasma wake in a plasma channel for special applications and control, *Phys. Plasmas* **23**, 053108 (2016).